A statistical comparison of solar wind sources of moderate and intense geomagnetic storms at solar minimum and maximum

Jichun Zhang,[1] Michael W. Liemohn,[1] Janet U. Kozyra,[1] Michelle F. Thomsen,[2] Heather A. Elliott,[3] and James M. Weygand[4]

Received 10 February 2005; revised 2 October 2005; accepted 1 November 2005; published 13 January 2006.

[1] Superposed epoch analyses of 549 storms are performed to make a comparison of solar wind features of geomagnetic storm events at solar minimum (July 1974 to June 1977; July 1984 to June 1987; July 1994 to June 1997) and solar maximum (January 1979 to December 1981; January 1989 to December 1991; July 1999 to June 2002). In this study, geomagnetic storms are defined by the pressure-corrected *Dst* (*Dst**) and classified into moderate storms (-100 nT $< Dst^* \leq -50$ nT) and intense storms ($Dst^* \leq -100$ nT). The average values of interplanetary magnetic field (IMF), solar wind plasma, NOAA/POES hemispheric power, *Kp*, and *Dst** are analyzed and compared among the different storm categories. During the main phase of storms in each category, the average solar wind plasma parameters and IMF components are disturbed and compressed by a relative high-speed plasma stream. It is shown that the peak of the average solar wind density leads the minimum *Dst** (the zero epoch time) by 4.3–7.0 hours, which is longer than the peak time difference (0.3–1.0 hour) between the average IMF B_s and $Dst^*_{\min}$. For intense storms at solar minimum, the average IMF B_y is greatly disturbed during both the main phase and the recovery phase. In addition, the average solar wind density is enhanced up to 28 cm^{-3}, but the average solar wind bulk flow in this storm category is lower than those in all other categories. A significant finding is that the average interplanetary causes of intense storms at solar minimum are found to be against the well-known empirical criteria ($B_s \geq 10$ nT or $VB_s \geq 5.0$ mV/m for $\geq$3 hours), having a long interval of average $B_s = \sim$10 nT with dual peaks separated by $\sim$4.0 hours. The interplanetary and solar origins of storms in the different storm categories are also discussed.

Citation: Zhang, J.-C., M. W. Liemohn, J. U. Kozyra, M. F. Thomsen, H. A. Elliott, and J. M. Weygand (2006), A statistical comparison of solar wind sources of moderate and intense geomagnetic storms at solar minimum and maximum, *J. Geophys. Res.*, *111*, A01104, doi:10.1029/2005JA011065.

1. Introduction

[2] As a main contributor to space weather, geomagnetic storms (also called magnetic storms or storms), especially intense ones, can severely affect space-borne and ground-based technological systems [e.g., *Allen et al.*, 1989; *Lundstedt*, 1992; *Boteler*, 1993; *Viljanen and Pirjola*, 1994]. It is thus important to investigate the causes of storms at the Sun and in the solar wind.

[3] Storms are primarily caused by sufficiently intense, long-duration, and southward interplanetary magnetic field (IMF) B_s events, associated with intense and long-lasting interplanetary electric fields [*Gonzalez et al.*, 1994; *O'Brien and McPherron*, 2000a]. Southwardly directed IMF can reconnect with the northward magnetic field at the Earth's magnetopause, through which the interplanetary electric field also penetrates into the magnetosphere. An intensified ring current is developed when plasma sheet particles, in the presence of a dawn-to-dusk global convection electric field across the magnetotail, are injected into the nightside inner magnetosphere. The ring current causes a reduction in the Earth's magnetic field in equatorial regions, which can be measured by magnetic indices like the *Dst* index.

[4] Solar activity and the topology of the heliospheric current sheet (HCS), which are highly dependent on different phases of the solar cycle, play crucial roles in eliciting storms. Figure 1 shows the 12-year observations of solar wind bulk flow speed (red/blue line) and density (green line) by the Ulysses spacecraft as a function of solar latitude. The solar wind speed is color-coded to indicate the polarity of the IMF. The sunspot number is shown in the bottom row. During extremely quiet solar conditions, or at solar minimum as shown on the left of Figure 1, the Sun's streamer belts are confined to the region around the helio-

[1]Space Physics Research Laboratory, University of Michigan, Ann Arbor, Michigan, USA.
[2]Los Alamos National Laboratory, Los Alamos, New Mexico, USA.
[3]Space Science and Engineering, Southwest Research Institute, San Antonio, Texas, USA.
[4]Institute of Geophysics and Planetary Physics, University of California, Los Angeles, Los Angeles, California, USA.

0148-0227/06/2005JA011065

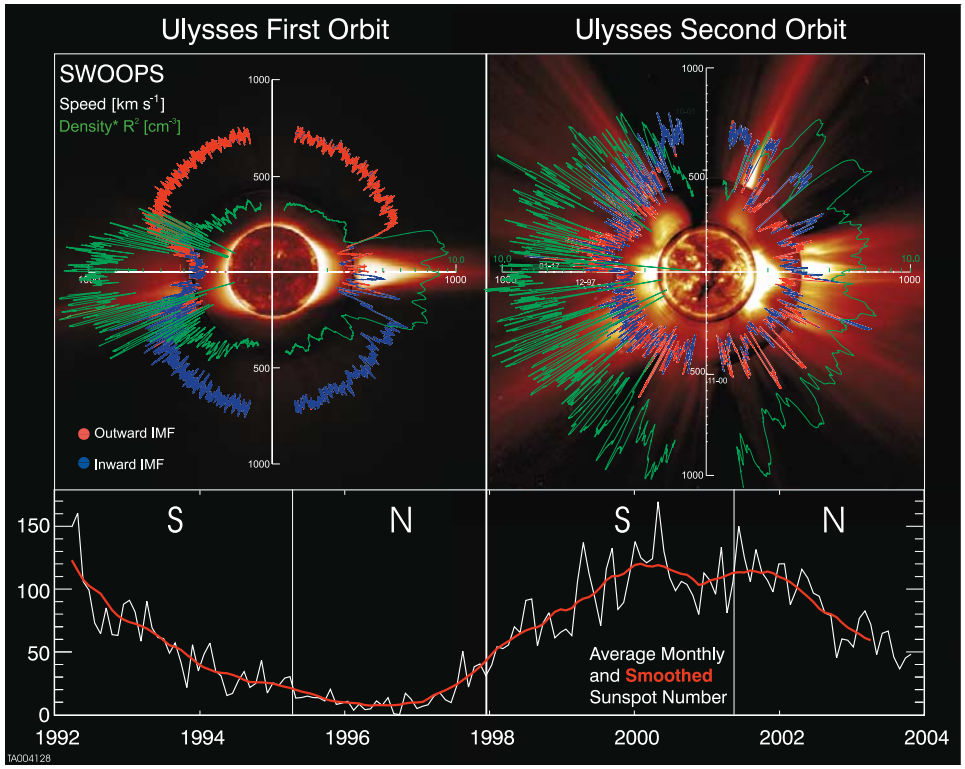

Figure 1. In the top row are polar plots of solar wind speed (white) and normalized density (green) as a function of latitude for Ulysses' first two orbits. The bottom panel shows the sunspot number. The IMF is color coded with the solar wind polarity: red for outward and blue for inward. The images of the sun in each panel are composed of three separate images. From the center out, these images are from the Solar and Heliospheric Observatory (SOHO) Extreme Ultraviolet Imaging Telescope (Fe XII at 195 Å), the Mauna Loa K-coronameter (700–950 nm), and the SOHO C2 Large Angle Spectrometric Coronagraph (white light). The first orbit spans solar minimum, and is plotted on top of solar images taken at solar minimum on 8/17/1996. Likewise, the second orbit spans solar maximum and is plotted on top of solar images taken at solar maximum on 12/07/2000. This figure is adapted from Plate 1 of *McComas et al.* [2000] and Figure 1 of *McComas et al.* [2003] to include recent measurements.

graphic equator, and large coronal holes (CHs) dominate the high-latitude ionosphere. The HCS (not shown) is relatively smooth and well behaved, which is topologically equivalent to a "ballerina skirt." When high-speed streams emanating from CHs interact with streams of lower speed, a solar wind structure called a corotating interaction region (CIR) is developed [*Smith and Wolf*, 1976]. The CIRs are organized about the HCS within 20 AU during solar minimum conditions [*Pizzo*, 1994]. CIRs can result in recurrent geomagnetic storms whose period is equal to the rotational rate of the Sun (the Bartels period), ~27 days as seen at the Earth [*Sheeley et al.*, 1976; *Burlaga and Lepping*, 1977; *Gonzalez et al.*, 1999; *Richardson et al.*, 2000; *Richardson et al.*, 2001; *Richardson et al.*, 2002]. *Feynman and Gu* [1986] found that recurrent storms occur most frequently in the declining phase of the solar cycle.

[5] During solar maximum conditions as shown on the right of Figure 1, the solar corona structure is far more complex, with polar coronal holes disappearing, and both streamers and small coronal holes observed at all heliolatitudes. The HCS becomes highly distorted with a severely warped topology and a highly inclined tilt [*Zhao and Webb*, 2003]. In this period, the Sun's activity is dominated by flares and erupting filaments, and their concomitant coronal mass ejections (CMEs). CMEs, of which one-third to one-half are magnetic clouds [*Gosling*, 1990; *Cane et al.*, 1997], play an overriding role in driving geomagnetic activity, especially strong storms [e.g., *Zhang and Burlaga*, 1988; *Gosling*, 1990; *Gosling et al.*, 1991; *Tsurutani and Gonzalez*, 1997; *Farrugia et al.*, 1997; *Richardson et al.*, 2000; *Zhang et al.*, 2004].

[6] Magnetic storms and their solar wind drivers have been investigated for more than a century. A lot of studies are dedicated to this type of space weather event. Among the recent publications are the statistical studies [e.g., *Gonzalez and Tsurutani*, 1987; *Clúa de Gonzalez et al.*, 1993; *Taylor et al.*, 1994; *Tsurutani et al.*, 1995; *Cliver et al.*, 1996; *Loewe and Prölss*, 1997; *Yokoyama and Kamide*, 1997; *Bravo et al.*, 1998; *Vennerstroem*, 2001; *Lyatsky and Tan*, 2003; *Huttunen and Koskinen*, 2004], reviews [e.g., *Feldstein*, 1992; *Gonzalez et al.*, 1994; *Kamide et al.*, 1998a; *Gonzalez et al.*, 1999; *Daglis et al.*, 2003], and proceedings (e.g., International Conference on Magnetic Storms, Rikubetsu, Hokkaido, Japan, 6–8 October 1994) [*Kamide*, 1997; *Tsurutani et al.*, 1997]. Especially in recent years, with the launches of the Wind and Advanced Composition Explorer (ACE) spacecrafts in November 1994 and in August 1997, respectively, high-quality and almost

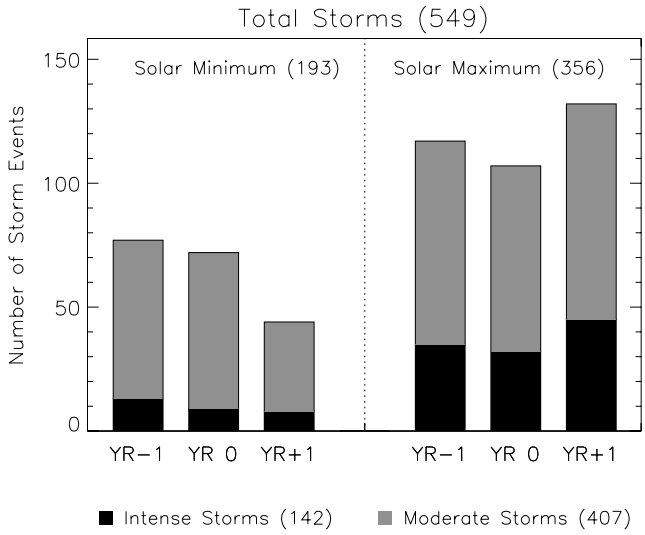

Figure 2. Histogram of the number of moderate and intense storm events in the three 3-year time periods of both solar minimum and solar maximum. The year with the monthly smoothed sunspot minimum or maximum is denoted by "YR 0." "YR − 1" ("YR + 1") is the year before (after) "YR 0." The total number of storms is given in the figure title. The numbers in subpanels indicate the subtotal of storms in each category.

continuous solar wind data are available. Solar wind observations from the Interplanetary Monitoring Platform (IMP)-8 spacecraft are also available as early as in 1973. It is therefore timely and valuable to study the solar activity dependence of the characteristics of storms and their solar wind sources by a statistical means with these abundant interplanetary observations. It is also interesting to investigate how the solar wind sources of different levels of storms are related to the Ulysses observations at the two solar extrema.

[7] In the present study, on the basis of the pressure-corrected *Dst* (*Dst**), we classify all storms at solar minimum and solar maximum of Solar Cycle 21, 22, and 23 into two sets, moderate and intense. The purpose of this paper attempts to establish the average behaviors of storm-time solar wind parameters in the four storm categories.

2. Event Selection

[8] Hourly *Dst* indices were downloaded from the World Data Center (WDC) C2, Kyoto and then corrected to remove the effects of the solar wind dynamic pressure [e.g., *Burton et al.*, 1975; *Gonzalez et al.*, 1989; *O'Brien and McPherron*, 2000a]:

$$Dst^* = Dst - bP_{dyn}^{1/2} + c,$$

where $b = 7.26\ nT/(nPa)^{1/2}$, $P_{dyn} = m_p\ nV^2$ which is solar wind dynamic pressure in nPa, and $c = 11\ nT$. Here m_p is the proton mass; n and V are hourly resolution solar wind number density and bulk flow speed, respectively.

[9] To calculate the so-called pressure-corrected *Dst* (*Dst**), the solar wind density n and bulk flow speed V data are from the OMNI data set in which all solar wind data are time-shifted from the spacecraft (e.g., IMP-8, Wind, and ACE) locations to the Earth.

[10] *Dst** is obtained by removing the contributions to the disturbance field at the Earth's surface from the magnetopause currents and thus contains mainly perturbations from near-Earth current systems, especially the inner magnetospheric contribution due to the ring current buildup and decay. In this paper, *Dst** is used to identify geomagnetic storms. According to the peak *Dst** value, the *Gonzalez et al.* [1994] storm intensity categories are applied:

$$\text{Moderate Storms} : -100\ \text{nT} < Dst^* \leq -50\ \text{nT}$$

$$\text{Intense Storms} : Dst^* \leq -100\ \text{nT}.$$

[11] Note that we are not removing the contribution to *Dst* from the induced currents in the Earth [e.g., *Dessler and Parker*, 1959; *Langel and Estes*, 1985] in order to maintain consistency in the classification scheme with *Gonzalez et al.* [1994]. If either solar wind density n or bulk flow speed V or both are missing, *Dst** cannot be computed and is replaced by *Dst* to define a storm.

[12] On the basis of the monthly averages of sunspot numbers, we have selected three 3-year time periods (July 1974 to June 1977; July 1984 to June 1987; July 1994 to June 1997) as solar minimum and another three 3-year periods (January 1979 to December 1981; January 1989 to December 1991; July 1999 to June 2002) as solar maximum for this study. They are the two extreme solar activity levels of Solar Cycle 21, 22, and 23, respectively. As shown in Figure 1, the solar minimum of Solar Cycle 23 is the time period when Ulysses moved anticlockwise from solar latitude $\sim 14^\circ$ south through the ecliptic plane and over the North Pole to $\sim 74^\circ$ north in its first solar polar orbit; the solar maximum of Solar Cycle 23 is when Ulysses moved from solar latitude $\sim 50^\circ$ south through the ecliptic plane and over the North Pole to $\sim 38^\circ$ north in the second solar polar orbit.

[13] Figure 2 shows the number of moderate and intense storm events at solar minimum and solar maximum. In total, 549 storms, 193 at solar minimum and 356 at solar maximum, are identified and analyzed in this study. In all of the storm events, there are 407 moderate storms and 142 intense storms. In Figure 2, it can be found that geomagnetic activity at solar maximum is much higher than that at solar minimum. Specifically, the 112 intense storms at solar maximum are almost four times those at solar minimum, of which the subtotal is 30.

[14] In this paper, the 549 storm events are classified into four categories by storm intensity and solar extrema: moderate storms at solar minimum, moderate storms at solar maximum, intense storms at solar minimum, and intense storms at solar maximum. The total storm number in each category is 163, 244, 30, and 112, respectively.

[15] Figure 3 demonstrates what is consistent with previous work [*Russell and McPherron*, 1973; *Crooker and Siscoe*, 1986; *Crooker et al.*, 1992; *Cliver and Crooker*, 1993; *Clúa de Gonzalez et al.*, 1993; *Gonzalez et al.*, 1999], that the storms in each category are more likely to occur near the equinoxes but are not limited to these times only. Two new features are also shown in Figure 3. One is that the occurrence percentage peaks of intense storms at either solar

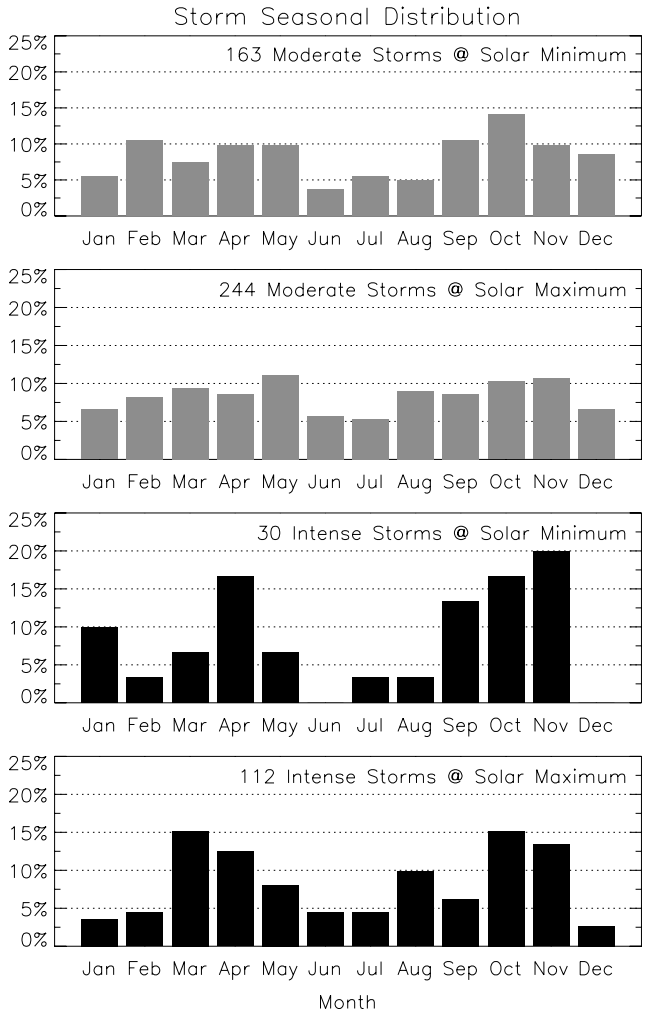

Figure 3. Monthly occurrence percentages of geomagnetic storms, as represented by the *Dst** index, in the four event categories. The subtotal of magnetic storms in each category is shown in the right upper corner of each panel.

maximum or solar minimum are greater than 15%, which is always not the case in moderate storms. In other words, intense storms have a more obvious seasonal distribution than moderate storms. The other feature is that half of the 30 intense storms at solar minimum appeared in September, October, and November.

3. Data Processing and Analysis

[16] Solar wind IMF and plasma in situ observations before 1995 are obtained from the IMP-8 spacecraft at the National Space Science Data Center (NSSDC); solar wind data during the January 1995 to June 1997 storms are from the Wind spacecraft and also obtained at the NSSDC; solar wind observations in the selected time period of July 1999 to June 2002 are ACE spacecraft in situ measurements (Level 2) downloaded from the ACE Science Center. Because the datum quality of Wind and ACE are better than that of IMP-8, the most recent solar wind data sets are from Wind and ACE. For the selected period of January 1995 to June 1997, Wind had an Earth orbit but entered the magnetosphere only a small fraction of the total time, ~3%. ACE is situated at the Sun–Earth Lagrange-1 (or L1) point and provides almost 100% observation coverage of the upstream solar wind conditions for the Earth.

[17] After they are transferred from the GSE to the GSM coordinate system with the GEOPACK software provided by N. A. Tsyganenko, solar wind observations are all propagated from the spacecraft locations to (17, 0, 0) R_E in the GSM coordinates with the minimum variance analysis (MVA) technique [*Weimer et al.*, 2003; *Weimer*, 2004]. All of the solar wind data sets are then averaged to 20-min resolution, taking any value which fell between the start minute and 20 min later, because with the 20-min temporal resolution the propagation error can be neglected and the Student's *t*-test (used below) becomes more reliable.

[18] Besides the *Dst* and *Dst** index, the global geomagnetic index *Kp* and the National Oceanic and Atmospheric Administration (NOAA)/POES Hemispheric Power are also used to study geomagnetic responses to solar wind disturbances. Three-hour resolution *Kp* indices are obtained from the World Data Center, Kyoto and linearly interpolated to the same resolution as the *Dst* index, 1 hour. The NOAA/POES Hemispheric Power data provide information about the estimated power in gigawatts deposited in the high-latitude ionosphere by energetic particles during transits over the poles by the NOAA POES (formerly called TIROS) satellites [*Fuller-Rowell and Evans*, 1987; *Evans*, 1987]. The NOAA/POES Hemispheric Power data lists (1979–2002) are downloaded from the NOAA website and then converted to 1-hour resolution without distinguishing the Hemispheric Power data in the Northern and Southern Hemispheres.

[19] Superposed epoch analyses of solar wind parameters, NOAA/POES Hemispheric Power, *Kp*, *Dst*, and *Dst** are performed for the four categories. The zero epoch time corresponds to the minimum *Dst** ($Dst^*_{\min}$) for each storm.

[20] Figure 4 shows the means of 36 superposed epoch analyses for the storm events in the four categories. The top eight panels show the superposed average values of IMF magnitude |B|, IMF B_x, $|B_x|$, B_y, $|B_y|$, B_z, the southward component of the IMF, B_s, and the eastward component of the interplanetary electric field VB_s. The bottom panel shows *Dst* variation which is denoted by the dotted line and *Dst** variation by the solid line. The zero epoch time is denoted by a vertical dotted line. The epoch time is from 1.5 days before the zero time to 1.5 days afterward. The Y axis in the B_s and VB_s panels is reversed for easier comparison with B_z. The horizontal dotted lines in the B_z panel denote zero values. The horizontal dot-dashed lines in B_z, B_s, and VB_s panels denote the thresholds for storms at the 80% occurrence level [*Gonzalez and Tsurutani*, 1987; *Gonzalez et al.*, 1994].

[21] Similar to Figure 4, Figure 5 shows the superposed epoch means of the solar wind plasma, NOAA/POES Hemispheric Power and geomagnetic indices for the storm events in the four categories. From top to bottom, the quantities in the seven panels are the superposed average values of solar wind plasma number density *n*, bulk flow speed *V*, dynamic pressure $Pdyn(= m_p\, nV^2)$, proton temperature *T* (at solar minimum, it is derived from the proton most probable thermal speed: $V_{th} = \sqrt{2kT/m_p}$), NOAA/

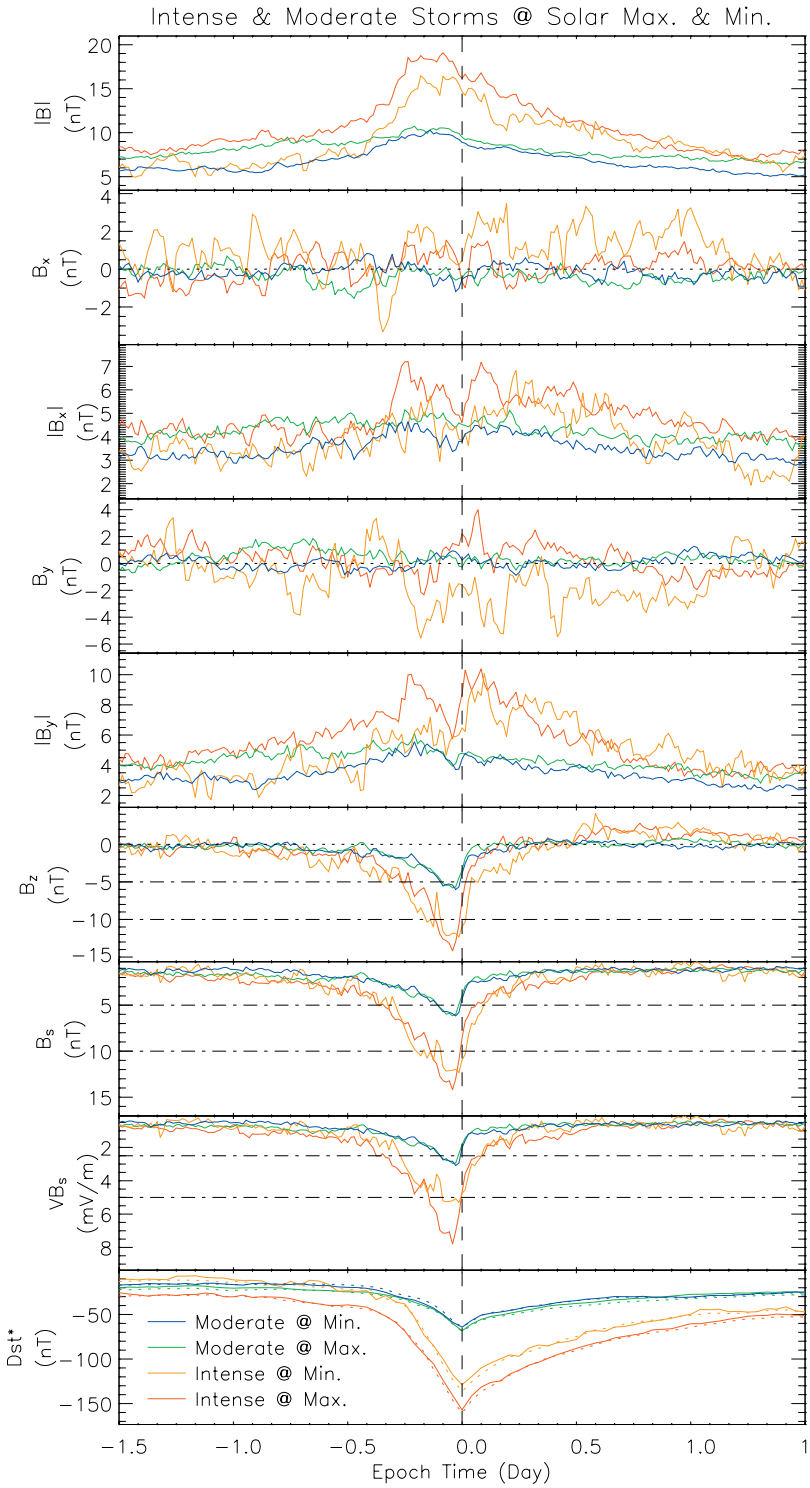

Figure 4. Superposed epoch means for storm events in the four categories. From top to bottom are plotted superposed average values of interplanetary magnetic field (IMF) magnitude $|B|$, IMF B_x, $|B_x|$, B_y, $|B_y|$, B_z, southward component of IMF B_s, eastward component of interplanetary electric field VB_s, and *Dst* variation denoted by the dotted line and *Dst** variation by the solid line. All data are in the GSM coordinate system. Zero on the epoch time axis corresponds to Dst^*_{min}, which is denoted by the vertical dotted line. The horizontal dotted lines in B_z panel denote zero values. The horizontal dot-dashed lines in B_z, B_s, and VB_s panels denote the thresholds for storms at the 80% occurrence level [*Gonzalez and Tsurutani*, 1987; *Gonzalez et al.*, 1994].

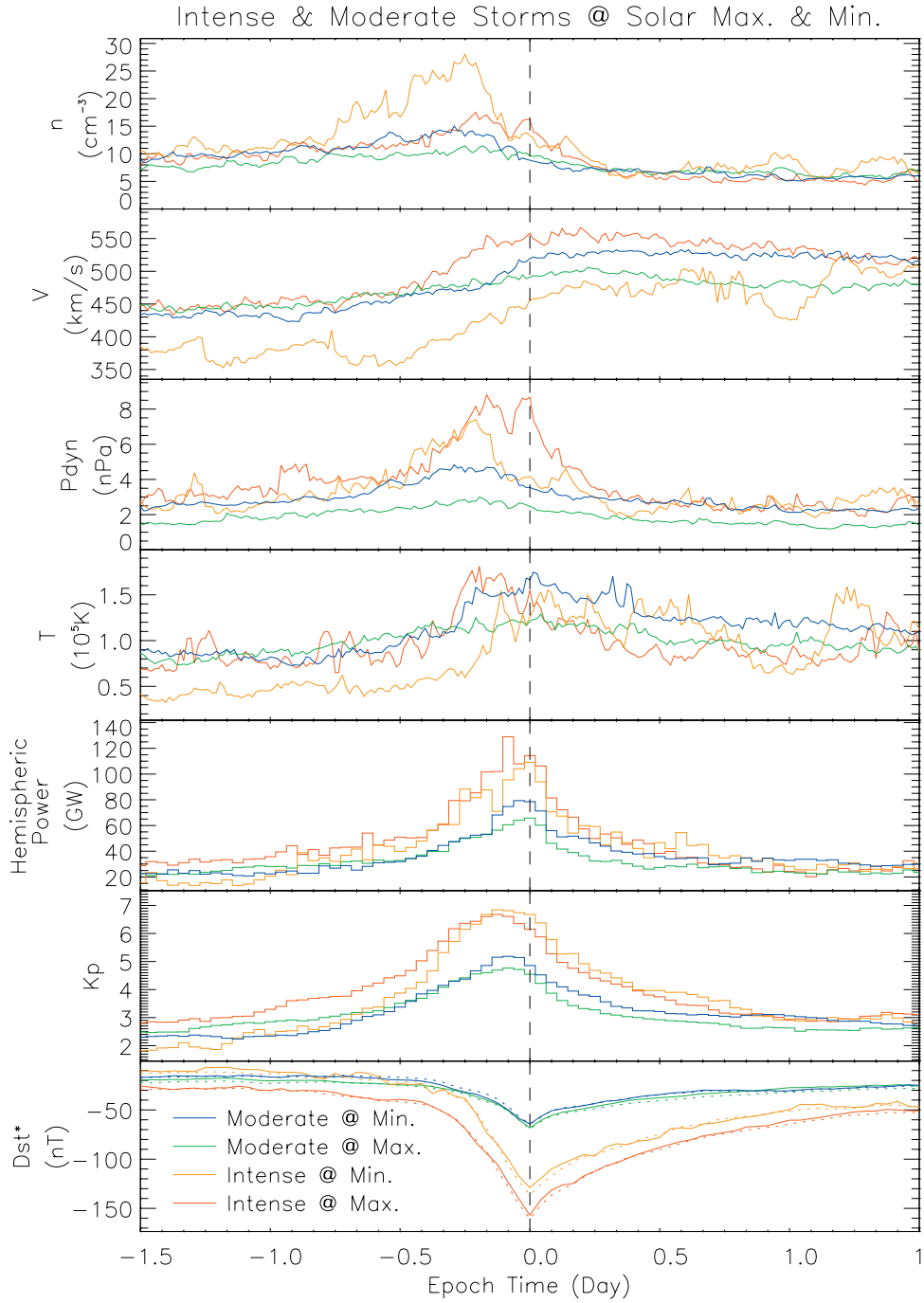

Figure 5. Same format as Figure 4, but from top to bottom are shown superposed average values of solar wind plasma number density *n*, bulk flow speed *V*, dynamic pressure *Pdyn*, proton temperature *T*, NOAA/POES Hemispheric Power, and ground-based geomagnetic *Kp*, and the *Dst* and *Dst** indices.

POES Hemispheric Power, and ground-based geomagnetic *Kp*, *Dst*, and *Dst** indices; for comparison, the average values of *Dst* and *Dst** are shown again.

[22] The medians, first quartiles, and third quartiles in this study are not shown but are available from the authors upon request. In every storm category, means and medians in each panel are not significantly different during the 3-day epoch time period except that means are almost always larger than medians in number density *n*, dynamic pressure *Pdyn*, and proton temperature *T*. This is because *n*, *Pdyn*, and *T* change on a log scale and their disturbances can significantly vary, even within the same level of geomagnetic activity. For example, the peak values of *n*, *Pdyn*, and *T* during the storm on 26 March 1995 ($Dst^*_{min} = -107.4$nT) are 74.4 cm^{-3}, 13.4 nPa, and 4.0 $\times$ 10^5 K, respectively. However, during the storm on 21 April 1997 ($Dst^*_{min} = -106.6$ nT), they are only 33.8 cm^{-3}, 8.9 nPa, and 9.7 $\times$ 10^5 K, respectively.

[23] To test the statistical significance of the means in Figures 4 and 5, we calculate the Student's *t*-statistic and its

Table 1. Student's *t*-Test for Peaks During Moderate Storms and Intense Storms Between at Solar Minimum and at Solar Maximum

		$\|B\|$	$\|B_y\|$	B_s	n	V	$Pdyn$	T	$Power$	Kp	Dst^*
Moderate	t[a]	−1.72	−0.46	0.29	1.12	1.43	2.50	2.10	2.95	4.42	2.35
	p[b]	0.086	0.645	0.771	0.263	0.153	0.013	0.037	3.50E-3	1.30E-5	0.020
Intense	t	−2.39	−1.59	0.10	2.19	−2.11	−2.09	−1.55	−1.93	0.69	1.90
	p	0.020	0.117	0.920	0.032	0.039	0.042	0.126	0.057	0.491	0.060

[a]Here t stands for the Student's t-statistic.
[b]Here p stands for the t-statistic's significance; a small value (<0.05) of p indicates that means are significantly different.

significance for each parameter at every time point among the four storm categories [*Reiff*, 1990]. The Student's t-statistic t of population x and y is the ratio of mean difference to the standard error of the differences, which is defined to be

$$t = \frac{\bar{x} - \bar{y}}{\sqrt{\dfrac{\sum_{i=0}^{M-1}(x_i - \bar{x})^2 + \sum_{i=0}^{N-1}(y_i - \bar{y})^2}{M + N - 2}\left(\dfrac{1}{M} + \dfrac{1}{N}\right)}},$$

where $x = (x_0, x_1, x_2, \ldots, x_{M-1})$ with mean $\bar{x}$ and $y = (y_0, y_1, y_2, \ldots, y_{N-1})$ with mean $\bar{y}$. The Student's t-test assumes that x and y have the same true variance. If x and y have very different variances, the difference of $\bar{x}$ and $\bar{y}$ may be difficult to interpret [*Press et al.*, 1992]. The significance of the Student's t-statistic, p, is determined by the incomplete ibeta function ($I_x(a, b) = \int_0^x u^{a-1}(1-u)^{b-1}du / \int_0^1 u^{a-1}(1-u)^{b-1}du$), the probability that the absolute value of t could be at least as large as the computed statistic given a random data set. The significance is a value in the interval [0.0, 1.0]; a small value (<0.05) indicates that the means of x and y are significantly different [*Miller*, 1986; *Press et al.*, 1992].

[24] Table 1 lists some results of the Student's t-test for the peaks of several parameters during moderate storms and intense storms between the two solar extrema, respectively. If peaks do not appear simultaneously, we do the Student's t-test for the peak value at solar maximum and the nonpeak value at the same epoch time at solar minimum.

4. Results: Similarities and Differences

4.1. Similarities

[25] Figure 4 and Figure 5 demonstrate the typical features of IMF, solar wind plasma, NOAA/POES Hemispheric Power, *Kp*, *Dst*, and *Dst** prior to and during both moderate storms and intense storms at solar minimum and solar maximum. Some features are in agreement with previous studies [e.g., *Gosling et al.*, 1972; *Hirshberg and Colburn*, 1973; *Gosling et al.*, 1991; *Gosling*, 1993; *Crooker and Cliver*, 1994; *Gonzalez et al.*, 1994; *Taylor et al.*, 1994; *Tsurutani et al.*, 1995; *Maltsev et al.*, 1996; *Loewe and Prölss*, 1997; *McAllister and Crooker*, 1997; *Pizzo*, 1997; *Yokoyama and Kamide*, 1997; *Crooker et al.*, 2000; *Lyatsky and Tan*, 2003], while others are present for the first time.

[26] In general, a typical storm begins with a storm gradual commencement (SGC) or a storm sudden commencement (SSC). An SSC is characterized by a sudden positive increase in the H component of the Earth's magnetic field when an interplanetary shockwave compresses the Earth's dayside magnetopause inward by several R_E. The SSC is followed by a period in which the elevated magnetic field does not change much (the initial phase). An SGC is when this *Dst* increase is absent. Following the initial phase is the storm's principal characteristic: the main phase, namely, an interval from one to several hours of large decrease of the *Dst* index. The storm concludes with the recovery phase, gradually returning to the normal level of the magnetic field H component over a period of hours to several days [*Gonzalez et al.*, 1994; *Kamide et al.*, 1998a]. These behaviors of the main phase and the recovery phase can be clearly seen in the bottom panel (*Dst* and *Dst**) of Figure 4. No SSC or initial phase can be seen in the *Dst* and *Dst** plot. The reason is that the minimum *Dst* or *Dst** may trail the SSC by a time period of from a few hours to 24 hours, and thus the SSCs and initial phase are necessarily smoothed out by the superposed epoch or averaging procedure taking $Dst^*_{\min}$ as a zero epoch. In addition, some storms do not have SSCs and more than half of storms undergo multiple-step main phase developments [*Kamide et al.*, 1998b], further smoothing the initial phase out of the average values. Moreover, the conversion from *Dst* to *Dst** removes the SSC signature because this is a magnetopause current effect.

[27] It is well known that the main phase of a geomagnetic storm is triggered by a southward IMF B_z turning [e.g., *Kokubun*, 1972] and exceeding some key threshold value [e.g., *Russell et al.*, 1974]. The duration of the IMF B_s also plays a crucial role in generating a magnetic storm [e.g., *Russell et al.*, 1974; *Gonzalez and Tsurutani*, 1987; *Gonzalez et al.*, 1994]. Figure 4 confirms the previously defined storm thresholds, for moderate storms, namely that there is $B_s \geq 5$ nT lasting for $\geq$2 hours, associated with interplanetary duskward electric fields $VB_s \geq 2.5$ mV/m for $\geq$2 hours [*Russell et al.*, 1974; *Gonzalez et al.*, 1994; *Zhang et al.*, 2004]. For intense storms, as shown in Figure 4, the interplanetary causes are different between the two solar extrema. We will discuss them in the next subsection.

[28] Around and after storm onset, the average IMF magnitude is enhanced; the three components (B_x, B_y, and B_z) of IMF, their derived values ($|B_x|$, $|B_y|$, and B_s), and eastward interplanetary electric field (VB_s) are all disturbed. By visual inspection of Figure 4, consistent with *Lyatsky and Tan* [2003], it can be found that by and large B_x and B_y anticorrelate (opposite signs) with each other during storms and their signs have no preference for causing storms at solar maximum and moderate storms at solar minimum. However, the signs of B_x and B_y during intense storms at solar minimum have a significant preference. That is, B_x (B_y) is strongly negative (positive) in the early main phase (~10 hours before $Dst^*_{\min}$) and almost always stays positive (negative) in the rest main phase and recovery phase; the Student's t-tests show that this feature is statistically significant, e.g., $t = -3.37$ and $p = 1.13$E-3. On average, negative B_z, B_s, and VB_s increase distinctly and strongly near storm

Table 2. $\overline{Dst^*_{min}}$[a] and Peaks of NOAA/POES Hemispheric Power and $\overline{Kp}$ in Each Storm Category

	$\overline{Dst^*_{min}}$	Hemispheric Power Peak		$\overline{Kp}$ Peak	
Storm Category	Value, nT	Value, GW	Preceding $\overline{Dst^*_{min}}$, hours	Value	Preceding $\overline{Dst^*_{min}}$, hours
Moderate at min.	−64.2 ±[b] 12.7	79.3 ± 33.2	1	5.2 ± 1.0	2
Moderate at max.	−68.3 ± 14.3	65.8 ± 31.8	0	4.8 ± 0.9	2
Intense at min.	−128.9 ± 33.2	109.1 ± 46.7	0	6.8 ± 1.1	3
Intense at max.	−157.0 ± 60.4	128.9 ± 67.8	2	6.7 ± 1.2	3

[a]The bars above the geomagnetic indices indicate average values.
[b]Here ±1 standard deviations are shown behind the plus-minus signs.

onset and remain enhanced throughout the main phase, with their peaks preceding those of the average *Dst* and *Dst** by less than 2 hours.

[29] Comparing Figure 5 to Figure 4, one can find that storms are tightly connected with increasing solar wind plasma parameters, too. Along with southward IMF B_z turnings or storm onsets, on average, bulk flow speed V, dynamic pressure *Pdyn*, and proton temperature T are also enhanced, but solar wind density begins to increase some hours earlier than others. These average features of the solar wind plasma are similar to a typical signature of the stream interface of a CIR. The peaks of solar wind density lead Dst^*_{min} by 4.3−7.0 hours, which are longer than the peak time differences (0.3−1.0 hour) between the primary storm drivers, B_z (also B_s and VB_s) and Dst^*_{min}. As far as timescales of the disturbances are concerned, it is illustrated on average in Figures 4 and 5 that solar wind bulk speed V and temperature T ramp up to larger values for a period of up to several days (the longest of any parameters); the IMF magnitude $|B|$ is enhanced for the next longest period; solar wind density n and dynamic pressure *Pdyn* are increased for about 1 day; the strong increases in negative IMF B_z, B_s, and VB_s last for almost half a day; IMF B_x and B_y components and their absolute values, $|B_x|$ and $|B_y|$, fluctuate with the shortest timescale sizes, that is, in minutes.

[30] Not surprisingly, the Hemispheric Power plot in Figure 5 shows that during storm activity, the auroral ovals become greatly disturbed with more energy from energetic particles deposited in the high-latitude ionosphere. On average, the Hemispheric Power is ∼20 gigawatts during magnetically quiet periods, but it is increased up to 79 gigawatts during moderate storms and 129 gigawatts during intense storms (quantitative peak values are also shown in Table 2 in the next subsection). This elevated activity in the high-latitude ionosphere during storms is also shown in the same figure in the variations of the *Kp* index.

4.2. Differences

[31] Figure 4 and Figure 5 also illustrate the differences of the average variations of IMF, solar wind plasma, NOAA/POES Hemispheric Power, *Kp*, *Dst*, and *Dst** among the four storm categories.

[32] As discussed in the last subsection, Figure 4 shows that solar minimum and solar maximum have the same thresholds of IMF B_s (≥5 nT) and its duration (≥2 hours) for moderate storms. One can also find in Figure 4 that intense storms at solar maximum are primarily caused by large IMF $B_s \geq 10$ nT fields with duration ≥3 hours and corresponding interplanetary dusk-dawn electric fields VB_s are larger than 5.0 mV/m over a period exceeding 3 hours, which is also consistent with *Gonzalez and Tsurutani* [1987], *Gonzalez et al.* [1994], and *Zhang et al.* [2004]. Nevertheless, for intense storms at solar minimum, the time duration of $B_s \geq 10$ nT lasts for only 2.5 hours, which is less than previous work based on a high solar activity interval. An examination of the solar wind for the individual storm events reveals that only about half of the storms agree with the well-known empirical criterion ($B_s \geq 10$ nT for ≥3 hours). The average B_s event in intense activity at solar minimum has a longer duration of $B_s = \sim 10$ nT with a dual peak profile, and the two peaks are separated by ∼4.0 hours and their values are lower than that eliciting intense activity at solar maximum. A similar feature can also be found in B_z and VB_s. VB_s for intense solar minimum is larger than 5.0 mV/m for only 2.0 hours. This interval is significantly less than previous work because the average bulk flow for this category is less than the other categories. In addition, VB_s and B_z also have the dual peak profile in the main phase of intense storms at solar maximum. However, the second peak is much more intense than the first one which is similar to the finding of *Yokoyama and Kamide* [1997], while the two peak values of B_s, B_z, and VB_s are comparable during intense storms at solar minimum.

[33] As shown in Figure 4, the average IMF magnitude is enhanced from ∼6 nT to different peak values in the four storm classes: 10.3 nT during moderate storms at solar minimum, 10.7 nT during moderate storms at solar maximum, 16.5 nT during intense storms at solar minimum, and 19.1 nT during intense storms at solar maximum. As shown in Table 1, the Student's t-test ($t = -1.72$ and $p = 0.086$) indicates that mean IMF of 10.3 nT for moderate storms at solar minimum is not significantly different from the mean IMF of 10.7 nT for moderate storms at solar maximum at a confidence level of 91.4%. The t-test ($t = -2.39$ and $p = 0.020$) also indicates that mean IMF of 16.5 nT for intense storms at solar minimum is significantly different from the mean IMF of 19.1 nT for intense storms at solar maximum. The average IMF B_x, $|B_x|$, B_y, and $|B_y|$ are more disturbed during intense activity than during moderate activity. The average B_x and B_y are especially disturbed even in the late recovery phase of intense storms at solar minimum. Similar to the findings of *Lyatsky and Tan* [2003] who used 1-hour solar wind observations and only stated the time lag between $|B_x|$ and $|B_y|$, in every storm category $|B|$, $|B_x|$, and $|B_y|$ reach their peaks in the main phase several hours before the maxima in $|B_z|$ (not shown), negative B_z, B_s, and VB_s. Average $|B_x|$ and $|B_y|$ also show a second clear peak in the recovery phase of intense storms at either solar minimum or solar maximum. Another feature, consistent with *Lyatsky and Tan* [2003], is that in each storm category, the peak values of $|B_y|$, B_s, and $|B_z|$ (not shown) are generally larger than that of $|B_x|$.

[34] As shown in Figure 5, the lowest solar wind parameter gradients, indicating that the corresponding parameters are least disturbed, appear in moderate activity at solar maximum. In intense activity at solar minimum, the solar wind density increase is the most pronounced, from $\sim$11 cm^{-3} to $\sim$28 cm^{-3}. However, the temperature is the lowest before storms and the average solar wind bulk flow is slower than those in the other storm categories except in the late recovery phase, increasing from only $\sim$360 km/s to $\sim$500 km/s. The corresponding average ram pressure peaks at 7.4 nPa with 1 hour earlier than the first pressure peak (8.8 nPa) and 5 hours earlier than the second one (8.7 nPa) in intense activity at solar maximum. During intense storms at solar maximum, the average solar wind density displays an increase from $\sim$10 cm^{-3} to $\sim$18 cm^{-3}, which is later than the solar minimum density rise but extends its enhancement into the early recovery phase. The average ram pressure therefore peaks closer to Dst^*_{min}. The average temperature does not show a characteristic profile of a rapid increase and a slow decay as in other storm categories but a fast growth-fast decay profile. On the basis of the Student's *t*-test, in general, all solar wind plasma features above are statistically significant; distinctly different means having large absolute values of the *t*-statistic $|t|$ and small probabilities ($p < 0.05$).

[35] In the plots of NOAA/POES Hemispheric Power, *Kp*, and *Dst** (also *Dst*) in Figure 5, although the average variations of each geomagnetic activity index exhibit very similar behaviors in the four categories, several different features are notable.

[36] During moderate storms, even though the average Dst^*_{min} at solar maximum is statistically lower ($t = 2.35$ at $p = 0.020$) than that at solar minimum, the NOAA/POES Hemispheric Power and *Kp* have significantly higher peak values at solar minimum than at solar maximum ($t = 2.95$ at $p = 3.50$E-3 and $t = 4.42$ at $p = 1.30$E-5, respectively). As to intense storms, as also shown in Table 1, the peak values of the three geomagnetic indices, especially *Kp*, at the two solar extrema are not significantly different from each other.

[37] Table 2 quantitatively gives the averaged Dst^*_{min} values, averaged peak values of NOAA/POES Hemispheric Power and *Kp*, and their preceding Dst^*_{min} time in each storm category. During moderate storms, the NOAA/POES Hemispheric Power peaks on average 1 hour earlier than Dst^*_{min} at solar minimum and at the same time as Dst^*_{min} at solar maximum; the *Kp* index peaks 2 hours earlier than Dst^*_{min} at the two solar extrema. As for intense storms, the time that the Hemispheric Power peak precedes Dst^*_{min} is 2 hours at solar maximum and 0 at solar minimum; the peak of the *Kp* index occurs prior to Dst^*_{min} by 3 hours either at solar minimum or at solar maximum. The peak values of the activity indices in Table 2 and the storm subtotals (see Figure 2) show that intense storms at solar maximum not only are more intense but appear more frequently than at solar minimum.

5. Discussion

[38] In this paper, with the superposed epoch technique, we have examined the average patterns of the upstream solar wind values, NOAA/POES Hemispheric Power, *Kp*, and *Dst** during moderate storms and intense storms at solar minimum and solar maximum of solar cycles 21, 22, and 23. The similarities and differences of those average behaviors among the four storm categories have important implications for the purpose of geomagnetic storm predictions.

[39] In this study, we have chosen the time period of 3 years approximately centered on the trough (crest) of the monthly smoothed sunspot numbers as solar minimum (maximum). The duration of solar minimum (maximum) therefore includes the "usual" solar minimum (maximum) [e.g., *Vennerstroem*, 2001] and a short period of the late (early) declining phase and the early (late) rising phase of the solar cycle. However, the intervals of the two solar extrema we defined are also shorter than that of some previous studies [e.g., *Clúa de Gonzalez et al.*, 1993].

[40] The superposed epoch curves in section 4 show that the average solar wind plasma and IMF during the main phase of both moderate storms and intense storms either at solar minimum or at solar maximum is disturbed and compressed by a relative high-speed plasma stream [*Gonzalez et al.*, 1999; *Vennerstroem*, 2001; *Lyatsky and Tan*, 2003]. Because of this compression, the IMF magnitude and solar wind plasma parameters exhibit strong and well-defined increases during geomagnetic activity. The density enhancement generally appears in the compressed region before and around the leading region of geoeffective solar wind structures like CMEs and CIRs, but the IMF B_z turns southward mostly within those structures themselves [*Zhang et al.*, 2004]. As a result, density peaks more than 3 hours earlier than B_z (also B_s and VB_s) does in the four storm categories. The statistical nature also indicates that average solar origin, and thus average interplanetary origin, of magnetic activity are different at the two solar extrema.

[41] Because solar wind observations are extracted only 1.5 days before and during storms, solar wind density, especially during intense storms, are higher than those from Ulysses. It is clearly displayed in Figure 1 that at solar minimum the solar wind above 30° solar latitude has uniformly high speed and low density, while low latitudes see mostly lower speed solar wind flows with higher densities [*McComas et al.*, 2000]. The high-density, low-speed streams are associated with the HCS, the region separating the magnetic fields of the solar system's north and south hemisphere. The simultaneous reversal in the signs of B_x and B_y especially during intense storms at solar minimum as seen in Figure 4, shows the reversal in the Parker spiral direction by $\sim$180° and the presence of the HCS. The solar wind flows at solar minimum are not the fastest as shown in the speed panel of Figure 5. Possible explanations are: many solar wind ejecta like CMEs or MCs are even faster than high-speed streams which are associated with CIRs; the zero epoch time, Dst^*_{min}, is not at CIR stream interfaces and both low-speed streams and high-speed streams thus contribute to speed averages at some epoch times.

[42] Because the IMF B_z component typically has large fluctuations within the CIRs [*Gonzalez et al.*, 1999], the B_s events causing storms at solar minimum have irregular profiles. The average interplanetary causes of intense storms at solar minimum have a long duration of average $B_s = \sim$10 nT with dual peaks separated by $\sim$4.0 hours but $B_s \geq$ 10 nT for only 2.5 hours, which is against the well-known empirical criterion ($B_s \geq 10$ nT for $\geq$3 hours). The

corresponding average VB_s also has a similar dual-peak profile but is even less in agreement with the criterion ($\geq$5 mV/m with duration $\geq$3 hours) for VB_s, causing intense storms because of the quite low solar wind flow speed. A similar but not so well-defined feature can also be found in a 4-min resolution plot (not shown) of the B_s events eliciting moderate storms at solar minimum, which is consistent with the empirical criterion ($B_s \geq 5$ nT for $\geq$2 hours) for moderate storms, though. As a result, the main phase of storms at solar minimum are supposed to have several developments, which are smeared out in the variations of geomagnetic indices because of the averaging procedure in this study.

[43] For intense storms, the second peak value in B_z, B_s, and VB_s is much larger than the first one at solar maximum, which suggests that the strength of energy injection into the ring current is much more intense in the second main phase development. However, the two peak values in B_z, B_s, and VB_s, or the strength of two energy injections into the ring current, are comparable in intense activity at solar minimum. Only the dual-peak profile with obviously different peak values is in agreement with *Yokoyama and Kamide* [1997] because the intense storms are not differentiated for the selected time period (1983–1991) in the work of *Yokoyama and Kamide* [1997] and thus storms at solar maximum play a dominant role. In addition, *Yokoyama and Kamide* [1997] found the average time shift between the two peaks is about 10.0 hours for intense storms and 6.0–8.0 hours for moderate storms, which are larger than those in this study (4.0–6.0 hours). This inconsistency is caused by a special means used in the superposed epoch analysis of *Yokoyama and Kamide* [1997]: stretched or contracted the main phases and the corresponding *Dst* values of individual storms with regard to the averages.

[44] Because of its high strength and long duration like B_z in the main phase, the IMF B_y may significantly affect intense activity through antiparallel merging at the flanks of the Earth's magnetosphere [e.g., *Crooker*, 1979; *Vennerstroem and Friis-Christensen*, 1987]. This may be especially true in the early main phase of intense storms at solar minimum when the average IMF B_x is strongly negative and B_y is positive; in the late main phase and recovery phase, B_x and B_y are almost always positive and negative, respectively. These sign preferences mean that intense storms at solar minimum occur more frequently in the sector with the IMF pointing away or toward the Sun. Because IMF has the favorable polarity, the Russell-McPherron effect can be increased [*Russell and McPherron*, 1973; *Crooker et al.*, 1992] and the dominated solar wind structures at solar minimum, CIRs, can be more geoeffective. This feature is useful in space weather prediction.

[45] Besides IMF B_y and B_z, it appears that solar wind density, with an average peak value of up to 28 cm^{-3} (as shown in Figure 5), can play an important role in causing intense storms at solar minimum. Several recent studies [e.g., *Borovsky et al.*, 1998; *Smith et al.*, 1999; *O'Brien and McPherron*, 2000b; *Shue and Kamide*, 2001; *Daglis et al.*, 2003; *Thomsen et al.*, 2003] have presented evidence that under certain conditions solar wind density can significantly and independently affect the solar wind-magnetospheric interactions through partially determining the plasma density in the plasma sheet and in turn influencing the strength of the ring current and auroral electrojets. In addition, *Lopez et al.* [2004] have found that high solar wind density can enhance compression ratios across the bow shock, which produce larger magnetosheath fields and thus increase the rate of magnetic flux transfer and solar wind energy across the dayside magnetopause. Therefore solar wind density can be a factor in geomagnetic activity under the right circumstances.

[46] During solar maximum conditions, CHs are still present, but the holes are small and do not extend from the Sun's poles to the equator as often as at solar minimum. As shown in Figure 1, the uniform solar wind structures at solar minimum, high speed and low density at high latitudes but low speed and high density at low latitudes, disappear at solar maximum. Most storms, especially intense ones, are due to the CMEs which are associated with the Sun's dominant activity, such as flares and disappearing filaments [e.g., *Zhang and Burlaga*, 1988; *Gosling*, 1990; *Gosling et al.*, 1991; *Tsurutani and Gonzalez*, 1997; *Farrugia et al.*, 1997; *Richardson et al.*, 2000; *Richardson et al.*, 2001; *Richardson et al.*, 2002]. As a result, the typical behaviors of solar wind plasma parameters are different from those at solar minimum. During either moderate storms or intense storms at solar maximum, the peaks of solar wind density and dynamic pressure precede the average $Dst^*_{\min}$ values by a shorter time than during storms at solar minimum. In the statistical investigation of *Zhang et al.* [2004], it was found that magnetic clouds (MCs), a subset of the CMEs, are the interplanetary origin of $\sim$70% of intense storms during high solar activity years. One of the identifying signatures of MCs is that the temperature in MCs is lower than the ambient solar wind temperature. This MC signature is shown in the average temperature variations during intense storms at solar maximum, which increase rapidly in the main phase and decay fast to low values in the recovery phase.

[47] Unlike those at solar minimum, the average interplanetary causes of storms at solar maximum are found to be in good agreement with the well-known empirical criterion, $B_s \geq 5\ nT$ (or $VB_s \geq 2.5$ mV/m) for $\geq$2 hours for moderate storms and $B_s \geq 10$ nT (or $VB_s \geq 5.0$ mV/m) for $\geq$3 hours for intense storms [*Russell et al.*, 1974; *Gonzalez and Tsurutani*, 1987; *Gonzalez et al.*, 1994]. Intense storms at solar maximum not only are more intense but occur more frequently than at solar minimum.

[48] The big peak value difference in the B_s (also B_z) or VB_s events causing intense storms at solar minimum and at solar maximum is due to both the much higher intensity of the activity at solar maximum and the event selection criterion that we do not limit the lower value of Dst^* for intense storms ($Dst^* \leq -100$ nT). It is of interest to further investigate the solar wind drivers using more refined levels of intense activity.

[49] With the NOAA/POES Hemispheric Power data, we have shown that the auroral ovals become greatly disturbed during storms and the NOAA/POES Hemispheric Power gives a good estimate of the intensity of storms like Dst^* (also Dst) and Kp. However, the peak of Kp precedes on average that of the Hemispheric Power and $Dst^*_{\min}$ by 1 to 3 hours, depending on geomagnetic and solar activity levels. Furthermore, there are inconsistencies in the average peak values of the Hemispheric Power, Kp, and $Dst^*_{\min}$ during moderate storms at the two solar extrema (higher $|Dst^*_{\min}|$

with lower peak values of the Hemispheric Power and *Kp*). A similar inconsistency can even be found in *Kp* during intense storms. However, the Student's *t*-test shows that it is not statistically significant. These features can by explained by the facts as follows: the Hemispheric Power is only a measurement of the high-latitude region activity (polar and auroral particle precipitation); the *Kp* index is obtained from 13 subauroral magnetometer stations and thus influenced not only by the ring current but also by the auroral electrojets, field-aligned currents, and other magnetospheric currents [*Bartels et al.*, 1939].

[50] As a future complement to this study, it would be useful to carry out similar superposed epoch analyses of solar wind sources of storms in the rising and declining phase of the solar cycle. In addition, taking different time points, e.g., storm sudden commencement (SSC) or 50% recovery of storms, as the zero epoch time will be considered in future studies. Geomagnetic storms are complex phenomena. For example, more than half of them exhibit two-step or multiple-step developments in the main phase [*Kamide et al.*, 1998b] or recovery phase [*Hamilton et al.*, 1988; *Kozyra et al.*, 1998; *Liemohn et al.*, 1999; *Dasso et al.*, 2002]. It is thus important to classify storms into more subsets to investigate the characteristic nature of the solar wind sources of those different types of storms. Plasma and magnetic field observations in the inner magnetosphere, e.g., at geostationary orbit, can also be used in statistical studies to further understand the physical processes of solar wind-magnetospheric interactions during storms.

6. Summary

[51] We summarize our survey of the 549 storms in the four categories as follows:

[52] 1. The storms in each storm category have a seasonal distribution, but the seasonal distribution of intense storms is more obvious than that of moderate storms and half of intense storms at solar minimum appeared in September, October, and November.

[53] 2. All IMF components, VB_s, and solar wind plasma parameters are enhanced during moderate and intense storms at solar minimum and maximum. However, the disturbance intensity is dependent on the levels of geomagnetic and solar activity and the enhancement timescales are much different, from minutes to several days. The IMF components and VB_s are more disturbed during intense storms than moderate storms, which is not always the case for the solar wind plasma parameters.

[54] 3. The thresholds of B_s and its duration are $\geq$5 nT and $\geq$2 hours for moderate storms at the two solar extrema and $\geq$10 nT and $\geq$3 hours for intense storms at solar maximum. However, for intense storms at solar minimum the time duration of $B_s \geq 10$ nT lasts for only 2.5 hours, which is inconsistent with the empirical criterion.

[55] 4. The superposed epoch curves of B_s, B_z, and VB_s display a double peak in the main phase of intense storms. The second peak is much more intense than the first one at solar maximum, while the two peak values are comparable at solar minimum.

[56] 5. $|B|$, $|B_x|$, and $|B_y|$ reach their peaks in the main phase several hours earlier than the maxima in $|B_z|$, negative B_z, B_s, and VB_s. $|B_x|$ and $|B_y|$ show obvious dual-peaks around Dst^*_{min} during intense storms at solar minimum and solar maximum.

[57] 6. B_x and B_y are anticorrelated (opposite signs) with each other during storms but there is no strongly preferred B_x and B_y direction toward or away from the Sun for storms at solar maximum or moderate storms at solar minimum. Intense storms of solar minimum, however, preferentially occur with $B_x < 0$ and $B_y > 0$ (away IMF sector) in the early main phase and $B_x > 0$ and $B_y < 0$ (toward IMF sector) in the late main phase and recovery phase.

[58] 7. Moderate activity at solar maximum has the least disturbed solar wind plasma parameters. In intense activity at solar minimum, the solar wind density increase is the most pronounced, the solar wind bulk flow is the slowest except in the late recovery phase, the temperature is the lowest before storms, and the ram pressure peaks 1-hour (5-hour) earlier than the first (second) pressure peak in intense activity at solar maximum. The temperature during intense storms at solar maximum increases rapidly and decreases quickly, but other storm categories display a rapid increase and slow decrease in temperature.

[59] 8. The peaks of solar wind density lead Dst^*_{min} by 4.3–7.0 hours, which are longer than the peak time differences between B_z, B_s, and VB_s and Dst^*_{min}, i.e., 0.3–1.0 hour.

[60] 9. Storm developments can be monitored well with the NOAA/POES Hemispheric Power like *Dst** (also *Dst*) and *Kp*, which exhibits similar behaviors in the four storm categories. However, the peak of the Hemispheric Power and *Kp* leads Dst^*_{min} by 0–3 hours, depending on the levels of geomagnetic and solar activity. Furthermore, during moderate storms at the two solar extrema, higher $|Dst^*_{min}|$ on average has lower peak values of Hemispheric Power and *Kp*.

[61] **Acknowledgments.** The solar wind and IMF data from the IMP-8 spacecraft were obtained from the National Space Science Data Center (NSSDC) in NASA Goddard Space Flight Center. The Wind data were also obtained from the NSSDC, and Justin Kasper at MIT provided guidance on using the Wind/SWE observations. The ACE MAG and SWEPAM instrument teams and the ACE Science Center supplied the level 2 ACE data available on the ACE Science Center Web site (http://www.srl.caltech.edu/ACE/ASC/). The *Dst* and *Kp* indices were provided by the World Data Center C2 at Kyoto University. Some solar wind density and bulk flow speed data used to calculate *Dst** were obtained from the OMNI Data Center. The NOAA/POES Hemispheric Power data were provided by Space Environment Center, NOAA, U.S. Department of Commerce. N. A. Tsyganenko provided GEOPACK, a group of FORTRAN subroutines for transformations between various coordinate systems. The Ulysses SWOOPS team provided Ulysses data and helped make Figure 1. The authors would like to thank the sources of funding for this study: NASA (under grants NAG5-10297, NAG5-11831, and NAG5-10850) and NSF (under grants ATM-0090165 and ATM-0402163). Work at Los Alamos was conducted under the auspices of the U. S. Department of Energy, with partial support from the NASA LWS program, under subcontract to the University of Michigan.

[62] Shadia Rifai Habbal thanks Ryuho Kataoka and another referee for their assistance in evaluating this paper.

References

Allen, J. H., L. Frank, H. Sauer, and P. Reif (1989), Effects of the March 1989 solar activity, *Eos, Trans. AGU*, *70*, 1479.

Bartels, J., N. H. Heck, and H. F. Johnston (1939), The three-hour-range index measuring geomagnetic activity, *J. Geophys. Res.*, *44*, 411.

Borovsky, J., M. Thomsen, and R. Elphic (1998), The driving of the plasma sheet by the solar wind, *J. Geophys. Res.*, *103*, 17,617.

Boteler, D. (1993), Geomagnetically induced currents: Present knowledge and future research, paper presented at IEEE PES Winter Meeting, Inst. of Electr. and Electron. Eng., Columbus, Ohio, 31 Jan. to 5 Feb.

Bravo, S., J. A. L. Cruz-Abeyro, and D. Rojas (1998), The spatial relationship between active regions and coronal holes and the occurrence of intense geomagnetic storms throughout the solar activity cycle, *Ann. Geophys.*, *16*, 49.

Burlaga, L. F., and R. P. Lepping (1977), The causes of recurrent geomagnetic storms, *Planet. Space Phys.*, *25*, 1151.

Burton, R. K., R. L. McPherron, and C. T. Russell (1975), An empirical relationship between interplanetary conditions and *Dst*, *J. Geophys. Res.*, *80*, 4204.

Cane, H. V., I. G. Richardson, and G. Wibberenz (1997), Helios 1 and 2 observations of particle decrease, ejecta, and magnetic clouds, *J. Geophys. Res.*, *102*, 7075.

Cliver, E. W., and N. U. Crooker (1993), A seasonal dependence for the geoeffectiveness of eruptive solar events, *Sol. Phys.*, *145*, 347.

Cliver, E. W., V. Boriakoff, and K. H. Bounar (1996), The 22-year cycle of geomagnetic and solar wind activity, *J. Geophys. Res.*, *101*, 27,091.

Clúa de Gonzalez, A. L., W. D. Gonzalez, and S. L. G. Dutra (1993), Periodic variations in geomagnetic activity: A study based on the Ap Index, *J. Geophys. Res.*, *98*, 9215.

Crooker, N. U. (1979), Dayside merging and cusp geometries, *J. Geophys. Res.*, *84*, 951.

Crooker, N. U., and E. W. Cliver (1994), A postmodern view of M regions, *J. Geophys. Res.*, *99*, 23,383.

Crooker, N. U., and G. L. Siscoe (1986), The effect of solar wind on the terrestrial environment, in *Physics of the Sun*, *Astrophysics and Solar-Terrestrial Relations*, *Geophys. Astrophys. Monogr.*, vol. III, edited by P. A. Sturrock et al., pp. 193–249, Springer, New York.

Crooker, N. U., E. W. Cliver, and B. T. Tsurutani (1992), The semiannual variation of great geomagnetic storms and the postshock Russell-McPherron effect preceding coronal mass ejecta, *Geophys. Res. Lett.*, *19*, 429.

Crooker, N. U., S. Shodhan, J. T. Gosling, J. Simmerer, R. P. Lepping, J. T. Steinberg, and S. W. Kahler (2000), Density extremes in the solar wind, *Geophys. Res. Lett.*, *27*, 3769.

Daglis, I. A., J. U. Kozyra, Y. Kamide, D. Vassiliadis, A. S. Sharma, M. W. Liemohn, W. D. Gonzalez, B. T. Tsurutani, and G. Lu (2003), Intense space storms: Critical issues and open disputes, *J. Geophys. Res.*, *108*(A5), 1208, doi:10.1029/2002JA009722.

Dasso, S., D. Gómez, and C. H. Mandrini (2002), Ring current decay rates of magnetic storms: A statistical study from 1957 to 1998, *J. Geophys. Res.*, *107*(A5), 1059, doi:10.1029/2000JA000430.

Dessler, A. J., and E. N. Parker (1959), Hydromagnetic theory of geomagnetic storms, *J. Geophys. Res.*, *64*, 2239.

Evans, D. S. (1987), Global statistical patterns of auroral phenomena, in *Proceedings of the Symposium on Quantitative Modeling of Magnetospheric-Ionospheric Coupling Processes*, edited by Y. Kamide, p. 325, Kyoto Sangyo Univ. Publ., Kyoto, Japan.

Farrugia, C. J., L. F. Burlaga, and R. P. Lepping (1997), Magnetic clouds and the quiet-storm effect at Earth, in *Magnetic Storms*, *Geophys. Monogr. Ser.*, vol. 98, edited by B. T. Tsurutani et al., pp. 91–106, AGU, Washington, D. C.

Feldstein, Y. I. (1992), Modelling of the magnetic field of magnetospheric ring current as a function of interplanetary parameters, *Space Sci. Rev.*, *59*, 83.

Feynman, J., and X. Y. Gu (1986), Prediction of geomagnetic activity on time scales of one to ten years, *Rev. Geophys.*, *24*, 650.

Fuller-Rowell, T. J., and D. S. Evans (1987), Height-integrated Pedersen and Hall conductivity patterns inferred from the TIROS-NOAA satellite data, *J Geophys. Res.*, *92*, 706.

Gonzalez, W. D., and B. T. Tsurutani (1987), Criteria of interplanetary parameters causing intense magnetic storms (*Dst* < −100 nT), *Planet. Space Sci.*, *35*, 1101.

Gonzalez, W. D., B. T. Tsurutani, A. L. C. Gonzales, E. J. Smith, F. Tang, and S.-I. Akasofu (1989), Solar wind magnetosphere coupling during intense magnetic storms, *J. Geophys. Res.*, *94*, 8835.

Gonzalez, W. D., J. Joselyn, Y. Kamide, H. Kroehl, G. Rostoker, B. Tsurutani, and V. Vasyliunas (1994), What is a geomagnetic storm?, *J. Geophys. Res.*, *99*, 5771.

Gonzalez, W. D., B. Tsurutani, and A. L. C. Gonzalez (1999), Interplanetary origin of geomagnetic storms, *Space Sci. Rev.*, *88*, 529.

Gosling, J. T. (1990), Coronal mass ejections and magnetic flux ropes in interplanetary space, in *Physics of Magnetic Flux Ropes*, *Geophys. Monogr. Ser.*, vol. 58, edited by C. T. Russell, E. R. Priest, and L. C. Lee, p. 343, AGU, Washington, D. C.

Gosling, J. T. (1993), The solar flare myth, *J. Geophys. Res.*, *98*, 18,937.

Gosling, J. T., A. J. Hundhausen, V. Pizzo, and J. R. Asbridge (1972), Compressions and rarefactions in the solar wind: Vela 3, *J. Geophys. Res.*, *77*, 5442.

Gosling, J. T., D. J. McComas, J. L. Phillips, and S. J. Bame (1991), Geomagnetic activity associated with Earth passage of interplanetary shock disturbances and coronal mass ejections, *J. Geophys. Res.*, *96*, 7831.

Hamilton, D. C., G. Gloeckler, F. M. Ipavich, W. Studemann, B. Wilken, and G. Kremser (1988), Ring current development during the great geomagnetic storm of February 1986, *J. Geophys. Res*, *93*, 14,343.

Hirshberg, J., and D. S. Colburn (1973), Geomagnetic activity at sector boundaries, *J. Geophys. Res.*, *78*, 3952.

Huttunen, K. E. J., and H. E. J. Koskinen (2004), Importance of post-shock streams and sheath region as drivers of intense magnetospheric storms and high-latitude activity, *Ann. Geophys.*, *22*, 1729.

Kamide, Y., (Ed.) (1997), Causes of Magnetic Storms, *J. Geophys. Res.*, *102*, 14029.

Kamide, Y., et al. (1998a), Current understanding of magnetic storms: Storm-substorm relationships, *J. Geophys. Res.*, *103*, 17,705.

Kamide, Y., N. Yokoyama, W. Gonzalez, B. Tsurutani, I. Daglis, A. Brekke, and S. Masuda (1998b), Two-step development of geomagnetic storms, *J. Geophys. Res.*, *103*, 6917.

Kokubun, S. (1972), Relationship of interplanetary magnetic field structure with development of substorm and storm main phase, *Planet. Space Sci.*, *20*, 1033.

Kozyra, J. U., M.-C. Fok, E. R. Sanchez, D. S. Evans, D. C. Hamilton, and A. F. Nagy (1998), The role of precipitation losses in producing the rapid early recovery phase of the Great Magnetic Storm of February 1986, *J. Geophys. Res.*, *103*, 6801.

Langel, R. A., and R. H. Estes (1985), Large-scale, near-field magnetic fields from external sources and the corresponding induced magnetic field, *J. Geophys. Res.*, *90*, 2487.

Liemohn, M. W., J. U. Kozyra, V. K. Jordanova, G. V. Khazanov, M. F. Thomsen, and T. E. Cayton (1999), Analysis of early phase ring current recovery mechanisms during geomagnetic storms, *Geophys. Res. Lett.*, *26*, 2845.

Loewe, C., and G. Prölss (1997), Classification and mean behavior of magnetic storms, *J. Geophys. Res.*, *102*, 14,209.

Lopez, R. E., M. Wiltberger, S. Hernandez, and J. G. Lyon (2004), Solar wind density control of energy transfer to the magnetosphere, *Geophys. Res. Lett.*, *31*, L08804, doi:10.1029/2003GL018780.

Lundstedt, H. (1992), Solar caused potential in gas-pipelines in southern Sweden, in *Proceedings of Solar-Terrestrial Workshop in Ottawa May 18–22*, edited by M. A. Shea, pp. 607–610, Natl. Oceanic and Atmos. Assoc., Silver Spring, Md.

Lyatsky, W., and A. Tan (2003), Solar wind disturbances responsible for geomagnetic storms, *J. Geophys. Res.*, *108*(A3), 1134, doi:10.1029/2001JA005057.

Maltsev, Y., A. Arykov, E. Belova, B. Gvozdevsky, and V. Safargaleev (1996), Magnetic flux redistribution in the storm time magnetosphere, *J. Geophys. Res.*, *101*, 7697.

McAllister, A. H., and N. U. Crooker (1997), Coronal mass ejections, corotating interaction regions, and geomagnetic storms, in *Coronal Mass Ejections*, *Geophys. Monogr. Ser.*, vol. 99, edited by N. Crooker, J. A. Joselyn, and J. Feynman, pp. 279–289, AGU, Washington, D. C.

McComas, D. J., B. L. Barraclough, H. O. Funsten, J. T. Gosling, E. Santiago-Muñoz, R. M. Skoug, B. E. Goldstein, M. Neugebauer, P. Riley, and A. Balogh (2000), Solar wind observations over Ulysses' first full polar orbit, *J. Geophys. Res.*, *105*, 10,419.

McComas, D. J., H. A. Elliott, N. A. Schwadron, J. T. Gosling, R. M. Skoug, and B. E. Goldstein (2003), The three-dimensional solar wind around solar maximum, *Geophys. Res. Lett.*, *30*(10), 1517, doi:10.1029/2003GL017136.

Miller, R. G. (1986), *Beyond ANOVA: Basics of Applied Statistics*. John Wiley, Hoboken, N. J.

O'Brien, T. P., and R. McPherron (2000a), An empirical phase space analysis of ring current dynamics: Solar wind control of injection and decay, *J. Geophys. Res.*, *105*, 7707.

O'Brien, T. P., and R. McPherron (2000b), Evidence against an independent solar wind density driver of the terrestrial ring current, *Geophys. Res. Lett.*, *27*, 3797.

Pizzo, V. J. (1994), Global, quasi-steady dynamics of the distant solar wind: 1. Origin of north-south flows in the outer heliosphere, *J. Geophys. Res.*, *99*, 4173.

Pizzo, V. J. (1997), Global modeling of CME propagation in the solar wind, in *Coronal Mass Ejections*, *Geophys. Monogr. Ser.*, vol. 99, edited by N. Crooker, J. A. Joselyn, and J. Feynman, pp. 261–267, AGU, Washington, D. C.

Press, W. H., S. A. Teukolsky, W. T. Vetterling, and B. P. Flannery (1992), *Numerical Recipes: The Art of Scientific Computing*, 2nd ed., Cambridge Univ. Press, New York.

Reiff, P. H. (1990), The use and misuse of statistics in space physics, *J. Geomagn. Geoelectr.*, *42*, 1145.

Richardson, I. G., E. W. Cliver, and H. V. Cane (2000), Sources of geomagnetic activity over the solar cycle: Relative importance of coronal

mass ejections, high-speed streams, and slow solar wind, *J. Geophys. Res.*, *105*, 18,203.
Richardson, I. G., E. W. Cliver, and H. V. Cane (2001), Sources of geomagnetic storms for solar minimum and maximum conditions during 1972–2000, *Geophys. Res. Lett.*, *28*, 2569.
Richardson, I. G., H. V. Cane, and E. W. Cliver (2002), Sources of geomagnetic activity during nearly three solar cycles (1972–2000), *J. Geophys. Res.*, *107*(A8), 1187, doi:10.1029/2001JA000504.
Russell, C. T., and R. L. McPherron (1973), Semiannual variation of geomagnetic activity, *J. Geophys. Res.*, *78*, 92.
Russell, C. T., R. L. McPherron, and R. K. Burton (1974), On the cause of geomagnetic storms, *J. Geophys. Res.*, *79*, 1105.
Sheeley, N. R., Jr., J. W. Harvey, and W. C. Feldman (1976), Coronal holes, solar wind streams and recurrent geomagnetic disturbances, 1973–1976, *Solar Phys.*, *49*, 271.
Shue, J., and Y. Kamide (2001), Effects of solar wind density on auroral electrojets, *Geophys. Res. Lett.*, *28*, 2181.
Smith, E. J., and J. W. Wolf (1976), Observations of interaction regions and corotating shocks between one and five AU: Pioneers 10 and 11, *Geophys. Res. Lett.*, *3*, 137.
Smith, J. P., M. F. Thomsen, J. E. Borovsky, and M. Collier (1999), Solar wind density as a driver for the ring current in mild storms, *Geophys. Res. Lett.*, *26*, 1797.
Taylor, J. R., M. Lester, and T. K. Yeoman (1994), A superposed epoch analysis of geomagnetic storms, *Ann. Geophys.*, *12*, 612–624.
Thomsen, M. F., J. E. Borovsky, R. M. Skoug, and C. W. Smith (2003), Delivery of cold, dense plasma sheet material into the near-Earth region, *J. Geophys. Res.*, *108*(A4), 1151, doi:10.1029/2002JA009544.
Tsurutani, B. T., and W. D. Gonzalez (1997), The interplanetary causes of magnetic storms, in *Magnetic Storms*, *Geophys. Monogr. Ser.*, vol. 98, edited by B. T. Tsurutani et al., pp. 77–89, AGU, Washington, D. C.
Tsurutani, B. T., W. D. Gonzalez, A. L. C. Gonzalez, F. Tang, J. K. Arballo, and M. Okada (1995), Interplanetary origin of geomagnetic activity in the declining phase of the solar cycle, *J. Geophys. Res.*, *100*, 21,717.
Tsurutani, B. T., , W. D. Gonzalez, Y. Kamide, and J. K. Arballo (Eds.) (1997), *Magnetic Storms*, *Geophys. Monogr. Ser.*, vol. 98, 266 pp., AGU, Washington, D. C.
Vennerstroem, S. (2001), Interplanetary sources of magnetic storms: A statistical study, *J. Geophys. Res.*, *106*, 175.
Vennerstroem, S., and E. Friis-Christensen (1987), On the role of IMF B_y in generating the electric field responsible for the flow across the polar cap, *J. Geophys. Res.*, *92*, 195.
Viljanen, A., and R. Pirjola (1994), Geomagnetically induced currents in the Finnish high-voltage power system, *Surv. Geophys.*, *14*, 308.
Weimer, D. R. (2004), Correction to "Predicting interplanetary magnetic field (IMF) propagation delay times using the minimum variance technique," *J. Geophys. Res.*, *109*, A12104, doi:10.1029/2004JA010691.
Weimer, D. R., D. M. Ober, N. C. Maynard, M. R. Collier, D. J. McComas, N. F. Ness, C. W. Smith, and J. Watermann (2003), Predicting interplanetary magnetic field (IMF) propagation delay times using the minimum variance technique, *J. Geophys. Res.*, *108*(A1), 1026, doi:10.1029/2002JA009405.
Yokoyama, N., and Y. Kamide (1997), Statistical nature of geomagnetic storms, *J. Geophys. Res.*, *102*(A7), 14,215.
Zhang, G., and L. F. Burlaga (1988), Magnetic clouds, geomagnetic disturbances, and cosmic ray decreases, *J. Geophys. Res.*, *93*, 2511.
Zhang, J.-C., M. W. Liemohn, J. U. Kozyra, B. J. Lynch, and T. H. Zurbuchen (2004), A statistical study of the geoeffectiveness of magnetic clouds during high solar activity years, *J. Geophys. Res.*, *109*, A09101, doi:10.1029/2004JA010410.
Zhao, X. P., and D. F. Webb (2003), Source regions and storm effectiveness of frontside full halo coronal mass ejections, *J. Geophys. Res.*, *108*(A6), 1234, doi:10.1029/2002JA009606.

H. A. Elliott, Space Science and Engineering, Southwest Research Institute, P. O. Drawer 28510, San Antonio, TX 78228-0510, USA.
J. U. Kozyra, M. W. Liemohn, and J.-C. Zhang, Space Physics Research Laboratory, University of Michigan, 2455 Hayward Street, Ann Arbor, MI 48109-2143, USA. (jichunz@umich.edu)
M. F. Thomsen, Los Alamos National Laboratory, MS D466, Los Alamos, NM 87545, USA.
J. M. Weygand, Institute of Geophysics and Planetary Physics, University of California, Los Angeles, Los Angeles, CA 90095-1567, USA.